FULL PAPER

Aromatic Nitroreduction

ADVANCED
FUNCTIONAL
MATERIALS

www.afm-journal.de

Atomic Pd on Graphdiyne/Graphene Heterostructure as Efficient Catalyst for Aromatic Nitroreduction

Jiaqiang Li, Lixiang Zhong, Lianming Tong,* Yue Yu, Qing Liu, Shuchen Zhang, Chen Yin, Liang Qiao, Shuzhou Li,* Rui Si,* and Jin Zhang*

With the maximum atom-utilization efficiency, single atom catalysts (SACs) have attracted great research interest in catalysis science recently. To address the following key challenges for the further development of SACs: i) how to stabilize and avoid the aggregation of SACs, ii) how to enhance the specific surface area and conductivity of supports, and iii) how to achieve scalable mass production with low cost, a SAC consisting of single Pd atoms anchored on well-designed graphdiyne/graphene (GDY/G) heterostructure (Pd_1/GDY/G) is synthesized. Pd_1/GDY/G exhibits high catalytic performance, as demonstrated by the reduction reaction of 4-nitrophenol. Furthermore, density functional theory calculation indicates that graphene in the GDY/G heterostructure plays a key role in the enhancement of catalytic efficiency owing to the electron transfer process, deriving from the gap between the Fermi level of graphene and the conduction band minimum of GDY. The GDY/G heterostructure is a promising support for the preparation of extremely efficient and stable SACs, which can be used in a broad range of future industrial reactions.

1. Introduction

Single atom catalysts (SACs) have recently emerged as promising heterogeneous catalysts in many industrially important reactions because of their high activity and selectivity.[1–7] Since

Dr. J. Q. Li, Prof. L. M. Tong, Y. Yu, Q. Liu, Dr. S. C. Zhang,
C. Yin, Prof. J. Zhang
Center for Nanochemistry
Beijing Science and Engineering Center for Nanocarbons
Beijing National Laboratory for Molecular Sciences
College of Chemistry and Molecular Engineering
Peking University
Beijing 100871, P. R. China
E-mail: tonglm@pku.edu.cn; jinzhang@pku.edu.cn

L. X. Zhong, Dr. L. Qiao, Prof. S. Z. Li
School of Materials Science and Engineering
Nanyang Technological University
Singapore 639798, Singapore
E-mail: LISZ@ntu.edu.sg

Dr. L. Qiao
College of Science
Changchun University
Changchun 130022, P. R. China

Prof. R. Si
Shanghai Synchrotron Radiation Facility
Zhangjiang Laboratory
Shanghai 201204, P. R. China
E-mail: sirui@sinap.ac.cn

Zhang and co-workers reported the first dispersion of single Pt atoms on FeO_x,[8] various types of SACs have been successfully designed and prepared.[1,5,9–13] The further development of SACs faces several key challenges,[4,14,15] including i) how to stabilize and avoid the aggregation of SACs during the fabrication, storage and catalytic reactions, ii) how to enhance the specific surface area and conductivity of supports, and iii) how to achieve scalable mass production with low cost.

Graphdiyne (GDY) is a 2D carbon material that only consists of sp and sp^2 hybridized carbon atoms with diacetylenic linkages ($-C\equiv C-C\equiv C-$) connecting adjacent benzene rings.[16,17] Recently, SACs that anchor single atoms on GDY through the strong d–π interaction between metal atoms and carbon–carbon triple bonds have aroused great interest.[18–22] The unique alkyne-rich structure not only endows GDY with many attractive properties,[23] but also makes GDY an ideal support for SACs because of the uniformly distributed pores and large binding energies to metal atoms.[24,25] That is different from previously reported SACs, in which single atoms can be alloyed with an inert metal to form single-atom alloy (SAA),[26] stabilized by coordinatively unsaturated metal oxide ion centers,[12] or bonded to nitrogen atoms or defects in carbon supports.[9,27–30]

Apart from the strong bonding or coordination between single atoms and the underlying supports, the high specific surface area (SSA) and conductivity of supports are essential factors for the enhancement of catalytic performance. Almost all the reported GDY-supported SACs used 3D GDY nanowall/sheets with thickness about dozens of nanometers, but only the surface of GDY could provide anchoring sites for metal atoms.[19,20,22,24] In order to maximize the anchoring sites in GDY, the SSA has to be increased by reducing the layer numbers of GDY. Despite high catalytic performance, the practical application of SACs on GDY in industrially important reactions requires the capability of massive production, lowered cost, and improved catalytic efficiency. Although the synthesis of few-layered GDY film with high quality has been reported,[31,32] it is still difficult to massively produce few-layered GDY and to fully use GDY for SACs with low cost.

Here, we report a SAC consisting of single Pd atoms anchored on well-designed GDY/graphene (GDY/G) heterostructure (Pd_1/GDY/G), in which few-layered GDY with high quality was synthesized by using liquid-exfoliated graphene as an epitaxy template. GDY acts as an anchoring layer for Pd

**ADVANCED
SCIENCE NEWS**

www.advancedsciencenews.com

**ADVANCED
FUNCTIONAL
MATERIALS**

www.afm-journal.de

atom's deposition and its few-layered structures make sure the full use of anchoring sites. The existence of graphene not only plays a role of epitaxy template to guarantee few-layered GDY synthesis, but also enhances the SSA and conductivity of GDY/G heterostructure due to its monoatomic layer and excellent electrical properties, respectively. Moreover, massive production of few-layered GDY with high quality was achieved due to the use of large-scale production and low cost of liquid-exfoliated graphene. Pd_1/GDY/G, Pd_1/GDY/G-1, and Pd_1/GDY/G-2 with 0.855, 0.151, and 0.272 wt% Pd were prepared, respectively. The content of Pd in Pd_1/GDY/G is about fourfold higher than previously reported Pd SAC supported by GDY nanosheets.[22] Pd_1/GDY/G exhibits excellent catalytic activity and high turnover frequency (TOF, defined here as the amount of reactant that is converted into product per min by 1 mmol of Pd) compared with previously reported Pd-based catalysts, including the Pd SAC. Theoretical results reveal that the outstanding conductive nature of graphene and its higher Fermi level than the conduction band minimum (CBM) of GDY play a key role of electron transfer layer which contributes to the surpassing catalytic activity of Pd_1/GDY/G.

The schematic illustration of the synthetic strategy of GDY/G heterostructure is depicted in **Figure 1**. Graphene sheets were prepared from graphite through liquid exfoliation and were dispersed in pyridine with a concentration of 0.25 mg mL^{-1} (Figure S1, Supporting Information). Then, Eglinton coupling reaction was carried out in the presence of hexaethynylbenzene (HEB) and $Cu(OAc)_2$ at room temperature. Thanks to the van der Waals (vdW) interaction and lattice match between GDY and graphene,[32] few-layered GDY grew on both sides of graphene sheets. The Pd_1/GDY/G was prepared through a wet chemistry, in which $Pd(NO_3)_2$ was used as a precursor and reacted with GDY/G at 373K for 1 h to generate the Pd_1/GDY/G samples after reduced by $NaBH_4$. The reduction of 4-nitrophenol (4-NP) to

4-aminophenol (4-AP) in the presence of $NaBH_4$ was used to value the catalytic activity of Pd_1/GDY/G.

2. Results and Discussion

Figure 2a shows the photograph of black powder like GDY/G heterostructure. The scanning electron microscope (SEM) image of GDY/G is shown in Figure 2b, in which GDY/G heterostructure maintains the morphology of graphene with thickness increased. The inset in Figure 2b represents the pristine graphene sheets. Atomic force microscope (AFM) image in Figure 2c revealed that the total thickness of GDY/G is about 8 nm, in which the two overlapped layers of GDY/G are 8.72 nm (Δh_1) and 8.01 nm (Δh_2), respectively. And the thickness of GDY film on one side of graphene is estimated to be about 2.5 nm considering the thickness of graphene sheets (2.91 nm, inset in Figure 2c). Besides the changing of thickness, the surface roughness of GDY/G is different from bare graphene, which can be observed from the Peak Force Error channel of AFM characterization (Figure S2, Supporting Information). The thickness of GDY/G increases along with the increasing loading amount of monomer (Figures S3 and S4, Supporting Information). Transmission electron microscope (TEM) images (Figure 2d; Figure S5, Supporting Information) confirmed that the morphology of GDY/G is consistent with that of graphene sheets, indicating the in-plane growth of GDY on graphene. For comparison, the GDY samples synthesized using the same method without graphene showed 3D amorphous structures (Figure S6, Supporting Information). The SSA of GDY/G was measured to be as high as 390.6 m^2 g^{-1}, more than threefold higher than that of pristine GDY powder (120.5 m^2 g^{-1}; Figure S7, Supporting Information) or other GDY samples.[33,34] In order to further demonstrate that GDY can grow on chemically exfoliated graphene using the same approach, we prepared
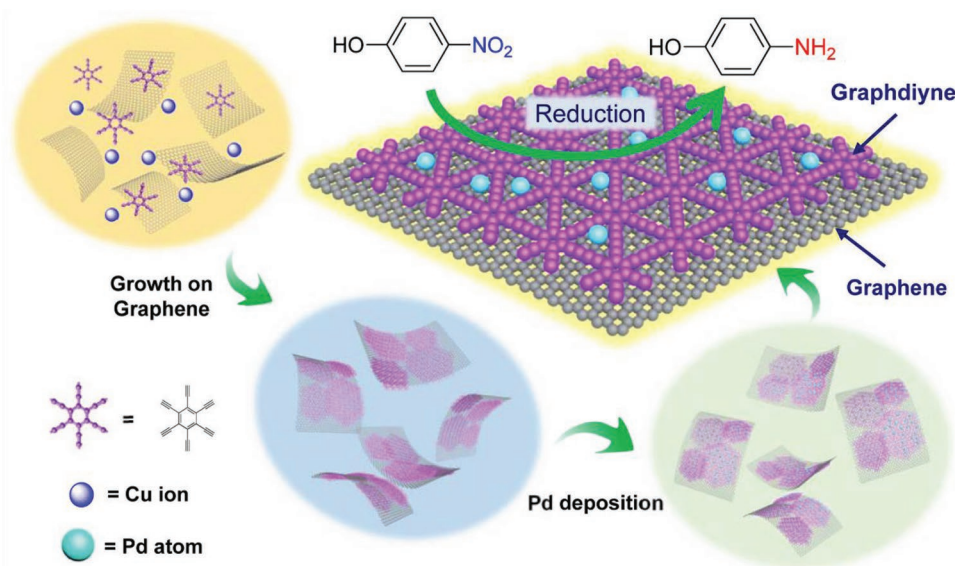

Figure 1. Schematic illustration of the experimental setup for the GDY/G heterostructure synthesis through a solution-based vdW epitaxy method, Pd_1/GDY/G preparation and catalyzed for 4-NP reduction.
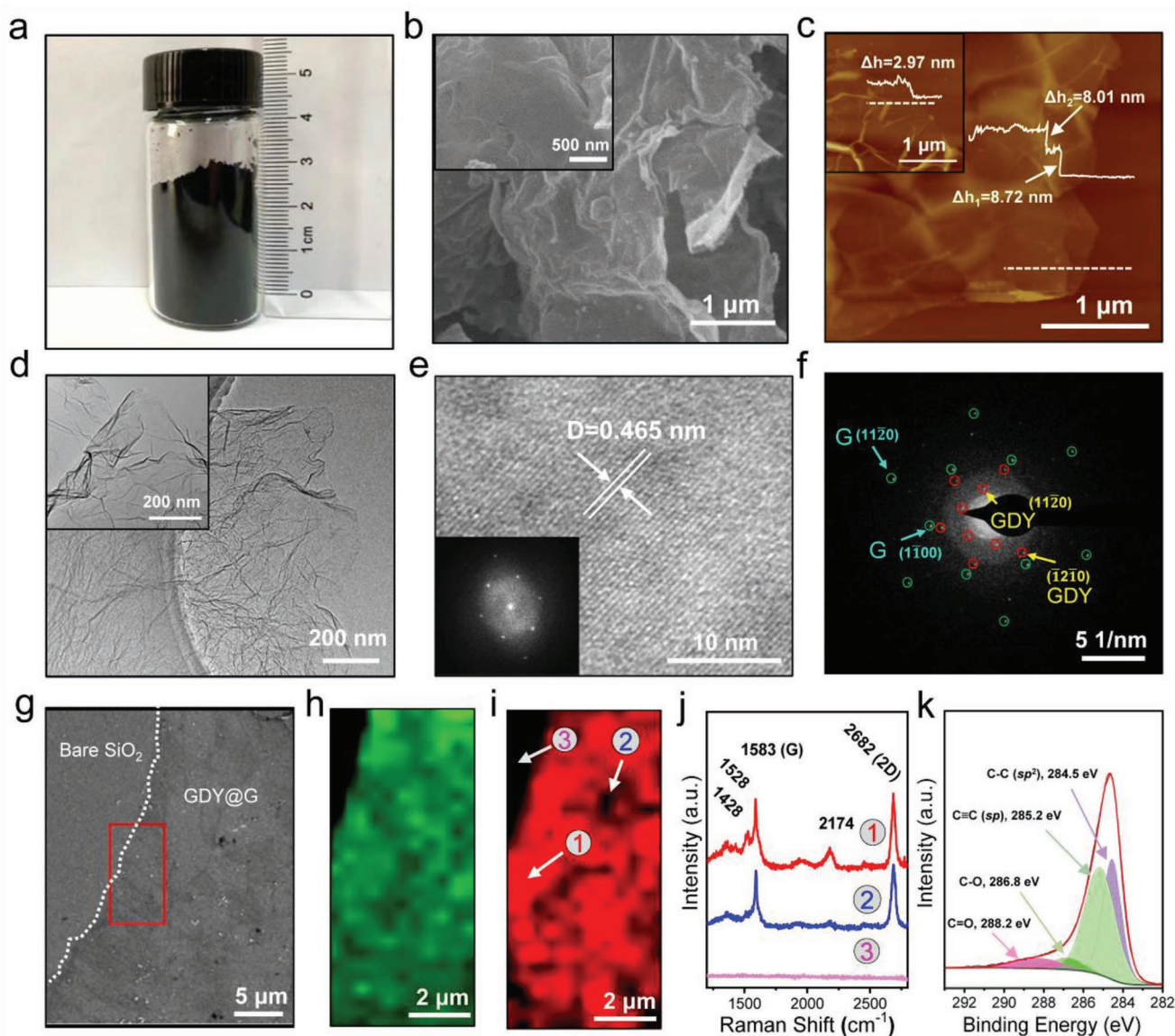
Figure 2. a) Image of bulk GDY/G powder. b–d) SEM, AFM, and TEM images of GDY/G. The insets show the corresponding images of graphene before the growth of GDY. The two overlapped layers of GDY/G are 8.72 and 8.01 nm ($\Delta h_1 = 8.72$ nm, $\Delta h_2 = 8.01$ nm, in (c)), respectively. e) HRTEM image of GDY synthesized on single layer graphene. The corresponding FFT pattern is shown in the inset. f) SAED image of as-synthesized GDY/G film, which shows that GDY and graphene films are both single crystalline. g) SEM image of GDY/G synthesized on single layer graphene. Raman mapping images of the 2D band (2682 cm^{-1}) of graphene h) and the carbon–carbon triple bond (2174 cm^{-1}) of GDY i) of the marked area in (g). j) Raman spectra in different positions in the select positions in (i). k) The narrow scan XPS spectra for element C 1s of GDY/G.

GDY/G heterostructure using single layer chemical vapor deposition (CVD)-grown graphene under the same conditions. High-resolution TEM (HRTEM) characterization revealed that the interval of ordered lattice fringe is 0.465 nm (Figure 2e), which is consistent with the reported results.[32,35] More importantly, the fast Fourier transformation (FFT) (Figure 2e inset) and selected area electron diffraction (SAED) (Figure 2f) patterns exhibit a typical hexagonal symmetric pattern,[32] demonstrating the high degree of crystallinity. Figure 2g shows a typical SEM image of a GDY/G film on SiO$_2$ plate. Raman mapping was performed in the selected area and shown in Figure 2h (2682 cm^{-1}, 2D band of graphene) and Figure 2i (2174 cm^{-1},

symmetric stretching mode of −C≡C−C≡C−), respectively. The 2D band of graphene distributed uniformly around the selected area; however, the carbon–carbon triple bonds are not very uniformly distributed. Figure 2j shows the typical Raman spectra at different positions. In the Raman spectrum at position 1, 1583 and 2682 cm^{-1} are assigned to the lattice vibration modes of graphene, and 2174 cm^{-1} is the vibration of carbon–carbon triple bonds of GDY,[32] which is consistent with earlier reports.[32,36,37] Distinct peak at 2174 cm^{-1} can be clearly seen in the Raman spectra of GDY/G using liquid-exfoliated graphene sheets as template (Figure S8, Supporting Information).[32] X-ray photoelectron spectroscopy (XPS) measurements indicated that

the GDY/G is mainly composed of carbon element (Figure S9, Supporting Information). The C 1s orbital that can be deconvoluted into four subpeaks are assigned to the C=C, C≡C, C—O, and C=O bonds (Figure 2k), respectively. Energy-dispersive spectroscopy (EDS) elemental mapping associated with TEM image shows that the carbon element is the dominant component (Figure S10, Supporting Information).

Pd$_1$/GDY/G was synthesized through a wet chemical approach. Before the reduction process, the single Pd atom anchoring on GDY/G (denoted as Pd$_1$/GDY/G-O) maintains the morphology of GDY/G with no obvious Pd clusters (Figures S11 and S12, Supporting Information). The aberration-corrected high-angle annular dark-field scanning transmission electron microscopy (HAADF-STEM) images for Pd$_1$/GDY/G-O display isolated bright dots

dispersing on the GDY/G surface (**Figure 3**a), which can be attributable to the single Pd atoms. Furthermore, the elemental mapping images reveal the homogeneous spatial distributions of carbon and Pd on GDY/G (Figure 3b inset; Figures S13 and S14, Supporting Information). X-ray adsorption fine structure (XAFS) spectroscopy was used to study the electronic structure and coordination environments of single Pd atoms in Pd$_1$/GDY/G-O, along with Pd foil and PdO as reference samples. According to the X-ray absorption near edge structure (XANES) profiles (Figure 3c), the edge of Pd$_1$/GDY/G-O shifted to higher energy compared to that of Pd foil, almost identical to that of PdO indicating that the Pd in Pd$_1$/GDY/G-O is all in an oxidation state. Figure 3d shows the Fourier transformed (FT) extended X-ray absorption fine structure (EXAFS)
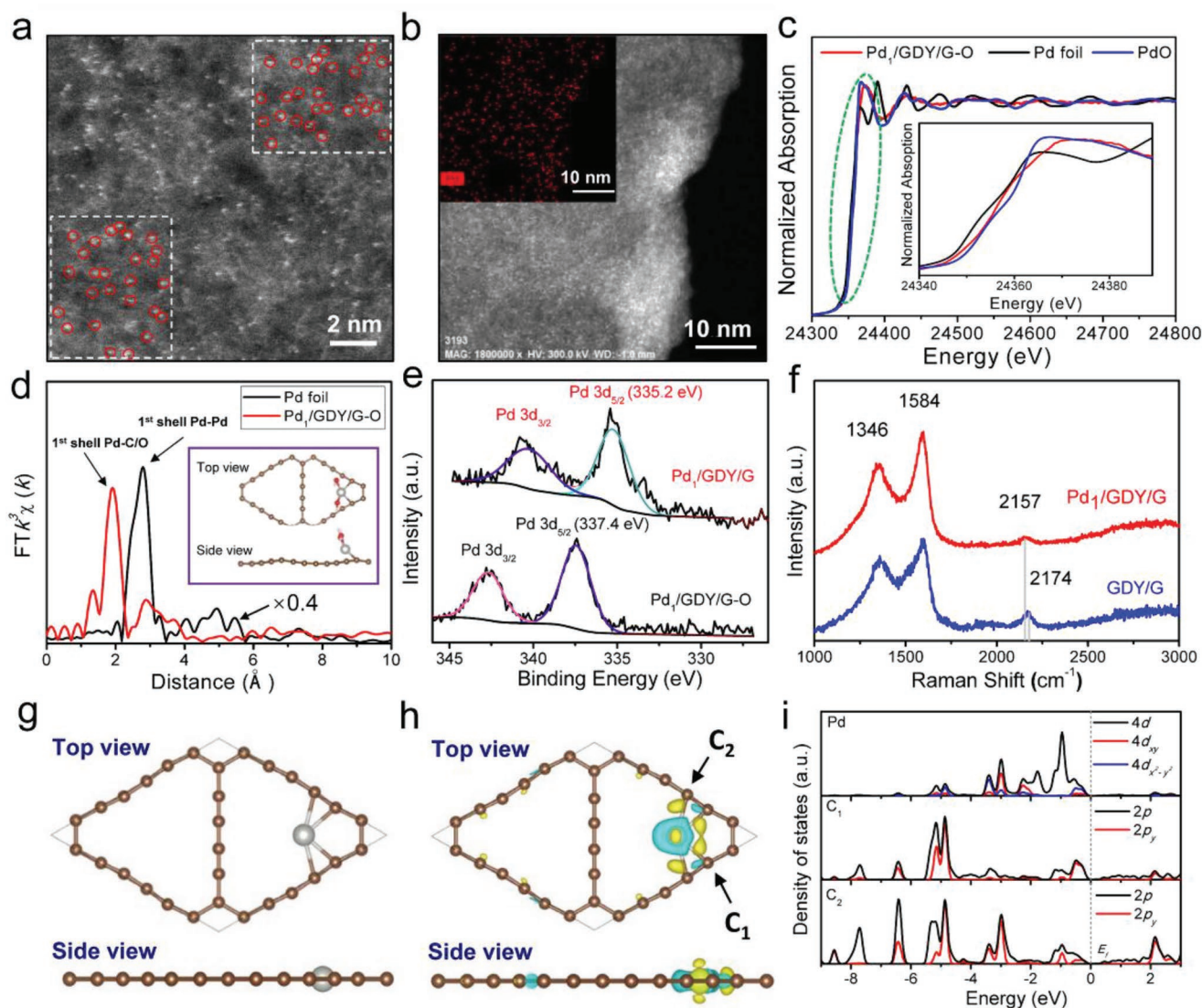

Figure 3. a) Atomic-resolution HAADF-STEM image of Pd$_1$/GDY/G-O. b) Elemental mapping for Pd$_1$/GDY/G-O. c) Pd K-edge XANES profiles of Pd$_1$/GDY/G-O, Pd foil, and Pd O (inset: expansion of the highlighted region). d) EXAFS spectra of Pd$_1$/GDY/G-O and Pd foil (inset: optimized geometric structure for the adsorption of the Pd^{2+} single atoms on GDY). e) High-resolution core level spectra of Pd 3d for Pt$_1$/GDY/G-O and Pd$_1$/GDY/G. f) Raman spectra of GDY/G and Pd$_1$/GDY/G. g) Top and side views of the geometric structures for the adsorption of the Pd single atoms at the C site on GDY. h) Top and side views of the charge density difference of GDY and graphene in GDY/G heterostructure. Depletion and accumulation spaces are revealed in blue and yellow, respectively. i) The PDOS comparison for Pd 4d and C 2p of C$_1$ and C$_2$ orbitals within Pd$_1$/GDY/G.

**ADVANCED
SCIENCE NEWS**
www.advancedsciencenews.com

**ADVANCED
FUNCTIONAL
MATERIALS**
www.afm-journal.de

spectra of $Pd_1/GDY/G$-O and Pd foil in R space. For $Pd_1/GDY/G$-O, the only distinct peak observed at 1.9 Å corresponds to the first coordination shell of Pd in a bonding configuration of Pd—C or Pd—O.[38,39] In contrast, for Pd foil, an appreciable peak at about 2.8 Å can be ascribed to the first shell Pd–Pd coordination. The above results demonstrate that abundant single Pd atoms are successfully dispersed on GDY/G support. Considering the difficulties in discriminating the C/O neighbors by EXAFS fittings and the Pd^{2+} precursor, we resorted to the density functional theory (DFT) calculations to determine the optimized structures of $Pd_1/GDY/G$-O (Figure S15, Supporting Information).

The valence state of Pd in Pd/GDY/G-O was reduced to zero valent after reduction by $NaBH_4$ (Figure S16, Supporting Information). The valence states of Pd/GDY/G-O and $Pd_1/GDY/G$ were investigated by XPS (Figure S17, Supporting Information). As shown in Figure 3e, the peaks of Pd $3d_{5/2}$ and $3d_{3/2}$ in $Pd_1/GDY/G$ shift to lower binding energy (335.2 and 340.8 eV) compared to those of $Pd_1/GDY/G$-O (337.4 and 342.7 eV), indicating the formation of zero-valent palladium (Pd^0) complexes.[22] The atomic-resolution HAADF-STEM image of $Pd_1/GDY/G$ illustrated that Pd atoms on the $Pd_1/GDY/G$ still maintain atomically dispersion without presence of any visible clusters or nanoparticles (NPs) (Figure S18, Supporting Information). The Raman spectra of GDY/G and $Pd_1/GDY/G$ where the Raman spectrum of $Pd_1/GDY/G$ presents a red shift and intensity decreasing compared with GDY/G (Figure 3f) indicate the formation of coordination bonds between Pd and carbon atoms of conjugated diyne linkers in GDY.[19] The calculated adsorption energies (Table S1, Supporting Information) indicate that Pd anchored on the corner site of the acetylenic ring (A site), which is the most preferred adsorption site for the Pd atoms on GDY among the investigated three cases (Figure 3g; Figure S19, Supporting Information).[19–22,25] Charge density difference map in Figure 3h indicates that significant electron redistribution occurs between the Pd atom and GDY structure, in which electrons are accumulated on GDY (yellow regions) and depleted around the Pd atom (blue regions). This electron redistribution implies strong interaction between the Pd atom and GDY. Figure 3i shows the projected partial density of states (PDOSs) of Pd 4d and C 2p of C_1 and C_2 orbitals, and the remarkable hybridization peaks around −3 and −5 eV below the Femi level confirm the relatively strong d–p coupling between Pd and C atoms.

Comparing with Pd nanoparticle-based catalysts, Pd SACs present higher surface area and more active sites, leading to higher catalytic efficiency and selectivity.[2,39–42] Catalytic hydrogenation of aromatic nitrocompounds to its corresponding amines is a very important reaction.[43–47] Considering the multiple steps for the reduction of nitro groups, there is a strong desire to develop highly chemoselective catalysts.[48] Inspired by the highly dispersed nature of single Pd atoms and the unique structure of GDY/G, we chose the reduction of 4-NP as a model reaction to value the catalytic activity of the $Pd_1/GDY/G$. The reduction process of 4-NP into the 4-AP was monitored by UV–vis spectroscopy at a given interval time. Upon the addition of $Pd_1/GDY/G$ into the mixture of 4-NP and $NaBH_4$, the absorption peak at 400 nm significantly decreased as the reaction proceeded (**Figure** 4a inset). Meanwhile, a new peak

appeared at 300 nm (Figures S20 and S21, Supporting Information), revealing the formation of 4-AP after the reduction of 4-NP. Figure 4a shows the time-dependent UV–vis absorption spectra recorded during the 4-NP reduction catalyzed by $Pd_1/GDY/G$, in which the absorption peak at 400 nm significantly decreases after 3 min. However, there is nearly no decreasing at 3 min when using commercial Pd/C as catalyst (Figure S22a, Supporting Information), which means that Pd/C presents much lower catalytic activity compared with $Pd_1/GDY/G$. The rate constant k of $Pd_1/GDY/G$ was calculated to be 0.953 min^{-1} that is about 44 times larger than that of Pd/C, indicating high catalytic reactivity of $Pd_1/GDY/G$ (Figure S22b, Supporting Information).[49] In order to demonstrate the effect of graphene, we prepared the Pd_1/GDY catalyst with 0.161 wt% Pd using bulk GDY powder as support and investigated its catalytic activity. The HAADF-STEM, elemental mapping, and XPS characterizations have proven that single Pd atoms are anchored on GDY (Figures S23 and S24, Supporting Information). Comparing the catalytic performance of Pd_1/GDY-1 which has very close Pd content (0.151 wt%) to Pd_1/GDY (Figure S25, Supporting Information), the absorption peaks at 400 nm catalyzed by Pd_1/GDY decreased slower than that of Pd_1/GDY-1 which means the relative lower catalytic activity of Pd_1/GDY (Figure 4b). The k of Pd_1/GDY is 0.0861 min^{-1}, less than half of $Pd_1/GDY/G$-1 (0.207 min^{-1}). Furthermore, the TOF of the $Pd_1/GDY/G$-1 is as high as 1762.17 min^{-1}, which is much higher than those of the Pd_1/GDY although the amount of Pd is comparable. These results demonstrate that graphene plays not only a role as epitaxy template for GDY growth, but also a key role of enhancing the catalytic activity for 4-NP reduction. Both of the TOF of $Pd_1/GDY/G$ and Pd/GDY/G-1 are much higher than that of previously reported Pd-based catalysts (Table S2, Supporting Information), including the Pd SAC using the graphene/amorphous carbon as support ($Pd_1/RGO@C$, 602.0 min^{-1}).[50]

Figure 4d shows that the 4-NP conversion remained at a constant value (>99%) without any decay during ten repeated catalytic cycles. Atomic-resolution HAADF-STEM results showed that the Pd atom still keeps mono dispersion as those in pristine $Pd_1/GDY/G$ (Figures S26 and S27, Supporting Information), suggesting its excellent stability. In order to demonstrate the scalability of the reduction of 4-NP using $Pd_1/GDY/G$, we designed a continuous reduction system to value the persistent catalytic activity of $Pd_1/GDY/G$ that would be further applied practically in water purification (Figure 4e). The color of 4-NP solution changed to colorless after filtrated by $Pd_1/GDY/G$ film at a flow rate of 8 mL min^{-1}. There is a distinct absorption peak at 400 nm in the upper solution owing to the nitrocompound (Figure 4f, blue curve). However, the distinct absorption peak at 400 nm disappeared and a new peak appeared at 300 nm in the lower solution, revealing the reduction of 4-NP and formation of 4-AP (Figure 4f, red curve). The continuous reduction phenomenon can be clearly observed in Video S1 in the Supporting Information. Figure 4g shows the absorbances of the lower solution at 300 and 400 nm, respectively. The absorbances of 4-NP at 400 nm did not increase over 20 h which means that there is no degradation of the catalytic activity. Obvious absorbance decreasing at 400 nm was observed after 30 h, indicating that the $Pd_1/GDY/G$ presents good catalytic activity in a long-term reduction process.
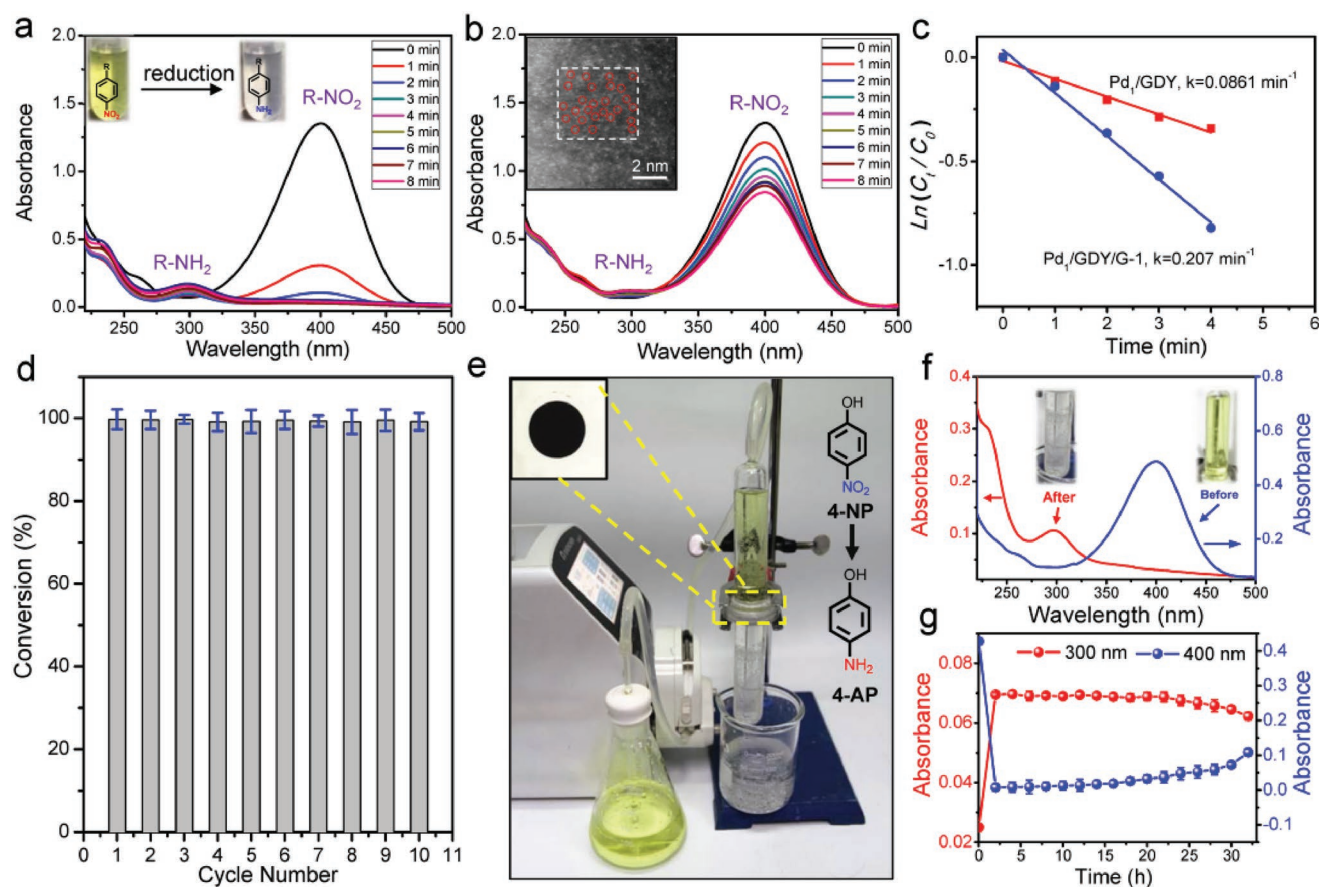
Figure 4. Time-dependent UV–vis absorption spectra recorded during the 4-NP reduction catalyzed by a) Pd$_1$/GDY/G and b) Pd$_1$/GDY. Corresponding atomic-resolution HAADF-STEM image of Pd$_1$/GDY is shown in the inset. c) Plots of ln(C_t/C_0) as a function of the reaction time for the reduction of 4-NP catalyzed by Pd$_1$/GDY/G-1 and Pd$_1$/GDY. d) Catalytic performance of Pd$_1$/GDY/G after ten catalytic cycles. e) Images of the setup of continuous flow to evaluate the catalyst performance in the 4-NP reaction. f) UV–vis absorption spectra recorded before (blue curve) and after (red curve) reduction in the continuous mode. g) The absorbances of the lower solution at 400 and 300 nm after reduction as a function of the reaction time.

Density functional theory calculations were performed to further understand the mechanism of 4-NP reduction and the role of graphene in Pd$_1$/GDY/G. The potential energy profiles along hydrogenation of 4-NP on Pd$_1$/GDY/G and Pd$_1$/GDY are shown in **Figure 5**a (black). The adsorption energy of 4-NP on Pd$_1$/GDY (denoted as Ar-NO$_2$*) is −0.43 eV (Figure S28, Supporting Information). The potential energy profiles indicate that the first hydrogenation of adsorbed 4-NP molecule (i.e., the formation of Ar-NOOH* intermediate) is the rate-limiting step. It is noticeable that all steps in the 4-NP reduction on Pd$_1$/GDY/G are completely downhill (Figure 5a, orange), indicating that the Pd$_1$/GDY/G could be more active toward 4-NP reduction compared with Pd$_1$/GDY. The potential energy profiles and hydrogenation route here demonstrate the superior catalytic activity of Pd$_1$/GDY/G than Pd$_1$/GDY in 4-NP reduction. The significant enhancement of catalytic activity of Pd$_1$/GDY/G might originate from the effect of graphene.

The electron energies of graphene and GDY are investigated theoretically to provide mechanism insights into the role of graphene (Figure 5b). The Fermi level of graphene (−4.35 eV relative to the vacuum level) is even higher than the CBM of GDY (−4.85 eV),[51] which indicates that electron will flow from graphene to GDY spontaneously in GDY/G heterostructure.

This phenomenon has been observed in other graphene-based heterostructures (e.g., MoS$_2$/graphene, graphene/C$_3$N$_4$, and graphene/N-doped MoS$_2$ heterostructures).[52–54] Charge density difference map indicates that electrons are accumulated on GDY (yellow regions) and depleted on graphene (blue regions) (Figure 5c,d), further confirming the electron transfer from graphene to GDY. Moreover, the high conductivity nature of graphene could facilitate the electron transportation within Pd$_1$/GDY/G composites. Considering the rate-determining step is adding the first hydrogen to the nitro, denoted as Ar-NO$_2$* + H$^+$ + e$^-$ = Ar-NOOH*, where H$^+$ comes from the solution and e$^-$ comes from the substrate. The extra electron transfer from graphene to GDY will increase the Fermi level of GDY and the energy of free electron (calculated to be 0.58 eV), which promotes the rate-determining step (II to III in Figure 5a) as well as the overall hydrogenation processes. The increased energy of electrons therefore leads to the total downhill in energy in the reduction process of 4-NP on Pd$_1$/GDY/G (Figure 5a, orange). Figure 5e schematically shows the overall proposed mechanism of 4-NP hydrogenation on Pd$_1$/GDY/G, where the 4-NP is reduced by electrons that are released from BH$_4^-$ and transferred from graphene network to GDY in the presence of hydrogen ions from the solution.
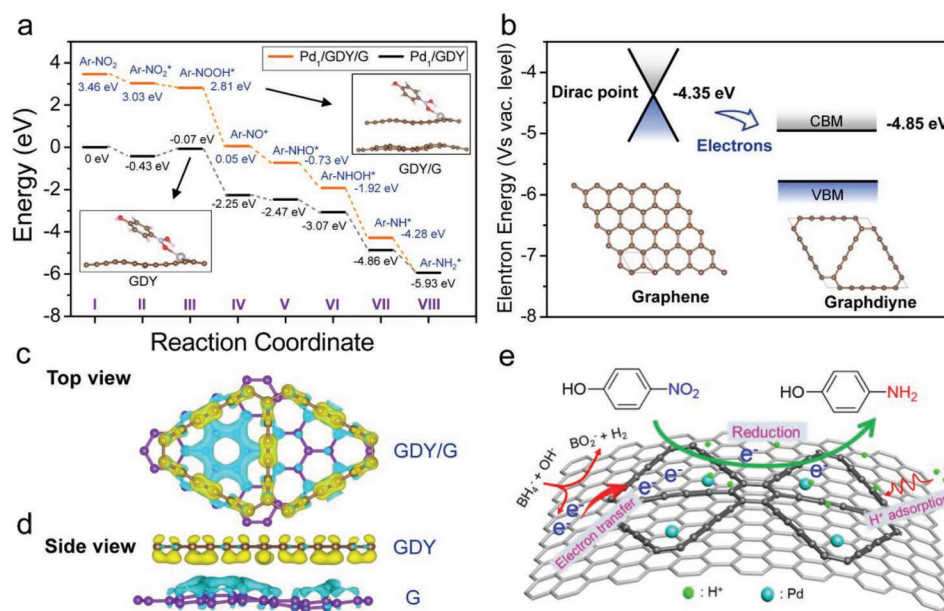
Figure 5. a) Potential energy profiles of 4-NP hydrogenation on $Pd_1/GDY/G$ and Pd_1/GDY (inset: optimized geometries of step III). For detailed optimized geometries from I to VIII, see Figure S28 in the Supporting Information. b) Electron energies of graphene and GDY. c) Top and d) side views of real space electron redistribution between graphene and GDY. e) Schematic illustration of the proposed mechanism of 4-NP reduction catalyzed by $Pd_1/GDY/G$.

3. Conclusion

In conclusion, we developed a novel vdW epitaxy method to synthesize GDY/G heterostructure, in which few-layered GDY with large-scale production is synthesized on liquid-exfoliated graphene by chemical method. Atomic Pd catalyst with Pd atoms anchored on GDY/G surface ($Pd_1/GDY/G$) was synthesized through a wet chemistry approach. The epitaxy-tempted role of graphene endows GDY/G heterostructure with high SSA that can provide much more metal atoms anchoring sites compared with the 3D GDY nanowall/sheets. Catalytic performance measurements revealed that $Pd_1/GDY/G$ presents remarkable catalytic activity and high stability for 4-NP reduction reaction. The conductive nature graphene in $Pd_1/GDY/G$ plays a necessary role of electron transfer in the reduction processes, which leads to higher catalytic activity compared with the atomic catalyst using pristine GDY as support.

4. Experimental Section

Synthesis of GDY/G Heterostructure: Hexaethynylbenzene solution was primarily synthesized through deprotection reaction of hexakis[(trimethylsilyl)-ethynyl]benzene (HEB-TMS). To a solution of hexakis[(trimethylsilyl)-ethynyl]benzene (100 mg) and dichloromethane (DCM, 20 mL), tetrabutylammonium fluoride (TBAF) (1 M in THF, 1 mL) was added under argon atmosphere and stirred at 0 °C for 15 min. Then, the mixture was washed two times with 50 mL deionized water, dried by anhydrous $MgSO_4$, and filtered. The HEB solution was added dropwise into a three-necked flask containing 10 mg graphene dispersed in 20 mL pyridine (5 mL), and 50 mg Cu(OAc)$_2$. The reaction mixture was maintained at room temperature for 20 h under argon atmosphere. All processes, from deprotection to addition, should be processed in dark, continuously, rapidly, and at low temperature to avoid decomposition of HEB. After the reaction completed, the GDY film was

grown on graphene sheets surface to form GDY/G heterostructure. After reaction completed, the GDY/G was washed in turn with pyridine, dimethylformamide (DMF), 1 M HCl, and deionized water. After free-drying, powder-like GDY/G heterostructure was obtained.

Synthesis of $Pd_1/GDY/G$: First, 10 mg GDY/G was dispersed into 30 mL deionized water in a 100 mL round-bottom flask, and the mixture was ultrasonically treated to obtain a homogenous suspension. Then, the pH value of GDY/G suspension was adjusted to about 10 by dropping 0.25 M Na_2CO_3 solution. Second, a certain amount of $Pd(NO_3)_2$ solution (containing 16 mg mL^{-1} $Pd(NO_3)_2$) was diluted into 10 mL water, and then the pH value of the solution was adjusted to 7 using 0.25 M Na_2CO_3. Subsequently, the pH neutral $Pd(NO_3)_2$ solution was introduced immediately to carbon support suspension dropwise under magnetic stirring at 100 °C, and then kept stirring at 100 °C for 1 h. At the end, the mixture was cooled to room temperature, collected by filter, and washed several times with deionized water, until it was free of Na^+ and CO_3^{2-}. Afterward, the $Pd_1/GDY/G$-O powders were reduced by 0.1 M $NaBH_4$ aqueous solution to obtain $Pd_1/GDY/G$ after vacuum drying at 60 °C for 12 h.

Measurement of the Catalytic Activity: In the case of batch experiments, the reduction of 4-NP was carried out in a quartz cuvette and monitored by using UV–vis spectroscopy at room temperature. The aqueous solution of $NaBH_4$ (0.4 mL, 0.2 M) and 4-NP (0.19 mL, 1×10^{-3} M) were mixed with water (1.41 mL). The mixture was stirred for 5 min at room temperature and then homogeneous dispersion of $Pd_1/GDY/G$ (30 μL, 0.5 mg mL^{-1}) was added. Each mixture was immediately subjected to UV–vis measurements and the spectra were recorded every 1 min to monitor the catalytic reduction reaction. In the case of continuous-flow reaction model, the continuous-flow 4-NP reductions were conducted in a tubular or fixed-bed microreactor. The catalyst (2 mg $Pd_1/GDY/G$) was packed in a quartz column reactor (2 cm internal diameter) and the mixture of the 4-NP (0.1×10^{-3} M) and $NaBH_4$ (40×10^{-3} M) was pumped through the column at a flow rate of 8 mL min^{-1}.

DFT Calculations: All the calculations were performed using density functional theory as implemented in the Vienna ab initio simulation package (VASP). The ion–electron interactions were treated with the projector-augmented wave (PAW) pseudopotentials, and the plane-wave basis set was cut off at 400 eV. The general gradient approximation

(GGA) parameterized by Perdew, Burke, and Ernzerhof (PBE) was used to describe the exchange-correlation functional in structural relaxations. The Heyd–Scuseria–Ernzerhof (HSE06) hybrid functional was adopted in the calculations of electronic structures. All structures were fully relaxed by a conjugate gradient method until the force component on each atom was less than 0.02 eV Å^{-1}, and the convergence criterion of total energy in the self-consistent field method was set to 10^{-5} eV. Monolayer graphdiyne unit cell was adopted in the simulations and the optimized lattice constant was 9.460 Å. The thickness of vacuum was 20 Å to make sure that there was no superficial interaction between different layers. The k-point grid used for the Brillouin zone integration was $5 \times 5 \times 1$ sampled by the Monkhorst–Pack scheme. A larger cell or more k-points yielded the same results in the test calculations. The energies of the intermediates in 4-NP hydrogenation were calculated referring to the energies of 4-NP, H_2, and H_2O.

Supporting Information

Supporting Information is available from the Wiley Online Library or from the author.

Conflict of Interest

The authors declare no conflict of interest.

[1] M. Yang, L. F. Allard, M. Flytzani-Stephanopoulos, *J. Am. Chem. Soc.* **2013**, *135*, 3768.
[2] P. Liu, Y. Zhao, R. Qin, S. Mo, G. Chen, L. Gu, D. M. Chevrier, P. Zhang, Q. Guo, D. Zang, B. Wu, G. Fu, N. Zheng, *Science* **2016**, *352*, 797.
[3] J. Lin, A. Wang, B. Qiao, X. Liu, X. Yang, X. Wang, J. Liang, J. Li, J. Liu, T. Zhang, *J. Am. Chem. Soc.* **2013**, *135*, 15314.
[4] H. Yan, C. Su, J. He, W. Chen, *J. Mater. Chem. A* **2018**, *6*, 8793.
[5] H. Fei, J. Dong, Y. Feng, C. S. Allen, C. Wan, B. Volosskiy, M. Li, Z. Zhao, Y. Wang, H. Sun, P. An, W. Chen, Z. Guo, C. Lee, D. Chen, I. Shakir, M. Liu, T. Hu, Y. Li, A. I. Kirkland, X. Duan, Y. Huang, *Nat. Catal.* **2018**, *1*, 63.
[6] C. H. Choi, M. Kim, H. C. Kwon, S. J. Cho, S. Yun, H. T. Kim, K. J. Mayrhofer, H. Kim, M. Choi, *Nat. Commun.* **2016**, *7*, 10922.
[7] Y. J. Chen, S. F. Ji, C. Chen, Q. Peng, D. S. Wang, Y. D. Li, *Joule* **2018**, *2*, 1242.
[8] B. Qiao, A. Wang, X. Yang, L. F. Allard, Z. Jiang, Y. Cui, J. Liu, J. Li, T. Zhang, *Nat. Chem.* **2011**, *3*, 634.
[9] C. Gao, S. Chen, Y. Wang, J. Wang, X. Zheng, J. Zhu, L. Song, W. Zhang, Y. Xiong, *Adv. Mater.* **2018**, *30*, 1704624.
[10] H. Wei, K. Huang, D. Wang, R. Zhang, B. Ge, J. Ma, B. Wen, S. Zhang, Q. Li, M. Lei, C. Zhang, J. Irawan, L. M. Liu, H. Wu, *Nat. Commun.* **2017**, *8*, 1490.
[11] P. Yin, T. Yao, Y. Wu, L. Zheng, Y. Lin, W. Liu, H. Ju, J. Zhu, X. Hong, Z. Deng, G. Zhou, S. Wei, Y. Li, *Angew. Chem., Int. Ed.* **2016**, *55*, 10800.
[12] Z. Zhang, Y. Zhu, H. Asakura, B. Zhang, J. Zhang, M. Zhou, Y. Han, T. Tanaka, A. Wang, T. Zhang, N. Yan, *Nat. Commun.* **2017**, *8*, 16100.
[13] H. B. Yang, S. F. Hung, S. Liu, K. D. Yuan, S. Miao, L. P. Zhang, X. Huang, H. Y. Wang, W. Z. Cai, R. Chen, J. J. Gao, X. F. Yang, W. Chen, Y. Q. Huang, H. M. Chen, C. M. Li, T. Zhang, B. Liu, *Nat. Energy* **2018**, *3*, 140.
[14] A. Wang, J. Li, T. Zhang, *Nat. Rev. Chem.* **2018**, *2*, 65.
[15] X. F. Yang, A. Wang, B. Qiao, J. Li, J. Liu, T. Zhang, *Acc. Chem. Res.* **2013**, *46*, 1740.
[16] M. M. Haley, S. C. Brand, J. J. Pak, *Angew. Chem., Int. Ed.* **1997**, *36*, 836.
[17] Y. Li, L. Xu, H. Liu, Y. Li, *Chem. Soc. Rev.* **2014**, *43*, 2572.
[18] T. He, S. K. Matta, G. Will, A. Du, *Small Methods* **2019**, *5*, 1800419.
[19] X. P. Yin, H. J. Wang, S. F. Tang, X. L. Lu, M. Shu, R. Si, T. B. Lu, *Angew. Chem., Int. Ed.* **2018**, *57*, 9382.
[20] Y. Xue, B. Huang, Y. Yi, Y. Guo, Z. Zuo, Y. Li, Z. Jia, H. Liu, Y. Li, *Nat. Commun.* **2018**, *9*, 1460.
[21] Z. Z. Lin, *Carbon* **2016**, *108*, 343.
[22] H. Yu, Y. Xue, B. Huang, L. Hui, C. Zhang, Y. Fang, Y. Liu, Y. Zhao, Y. Li, H. Liu, Y. Li, *iScience* **2019**, *11*, 31.
[23] M. Long, L. Tang, D. Wang, Y. Li, Z. Shuai, *ACS Nano* **2011**, *5*, 2593.
[24] D. W. Ma, T. Li, Q. Wang, G. Yang, C. He, B. Ma, Z. Lu, *Carbon* **2015**, *95*, 756.
[25] J. He, S. Y. Ma, P. Zhou, C. X. Zhang, C. He, L. Z. Sun, *J. Phys. Chem. C* **2012**, *116*, 26313.
[26] H. Zhou, X. Yang, L. Li, X. Liu, Y. Huang, X. Pan, A. Wang, J. Li, T. Zhang, *ACS Catal.* **2016**, *6*, 1054.
[27] W. Liu, L. Zhang, W. Yan, X. Liu, X. Yang, S. Miao, W. Wang, A. Wang, T. Zhang, *Chem. Sci.* **2016**, *7*, 5758.
[28] X. Wang, W. Chen, L. Zhang, T. Yao, W. Liu, Y. Lin, H. Ju, J. Dong, L. Zheng, W. Yan, X. Zheng, Z. Li, X. Wang, J. Yang, D. He, Y. Wang, Z. Deng, Y. Wu, Y. Li, *J. Am. Chem. Soc.* **2017**, *139*, 9419.
[29] W. Liu, L. Zhang, X. Liu, X. Liu, X. Yang, S. Miao, W. Wang, A. Wang, T. Zhang, *J. Am. Chem. Soc.* **2017**, *139*, 10790.
[30] H. Fei, J. Dong, M. J. Arellano-Jimenez, G. Ye, N. Dong Kim, E. L. Samuel, Z. Peng, Z. Zhu, F. Qin, J. Bao, M. J. Yacaman, P. M. Ajayan, D. Chen, J. M. Tour, *Nat. Commun.* **2015**, *6*, 8668.
[31] J. Zhou, J. Li, Z. Liu, J. Zhang, *Adv. Mater.* **2019**, e1803758, https://doi.org/10.1002/adma.201803758.
[32] X. Gao, Y. H. Zhu, D. Yi, J. Y. Zhou, S. S. Zhang, C. Yin, F. Ding, S. Q. Zhang, X. H. Yi, J. Z. Wang, L. M. Tong, Y. Han, Z. F. Liu, J. Zhang, *Sci. Adv.* **2018**, *4*, eaat6378.
[33] S. Zhang, H. Liu, C. Huang, G. Cui, Y. Li, *Chem. Commun.* **2015**, *51*, 1834.
[34] J. Li, J. Xu, Z. Xie, X. Gao, J. Zhou, Y. Xiong, C. Chen, J. Zhang, Z. Liu, *Adv. Mater.* **2018**, *30*, 1800548.
[35] C. Li, X. Lu, Y. Han, S. Tang, Y. Ding, R. Liu, H. Bao, Y. Li, J. Luo, T. Lu, *Nano Res.* **2018**, *11*, 1714.
[36] S. Zhang, J. Wang, Z. Li, R. Zhao, L. Tong, Z. Liu, J. Zhang, Z. Liu, *J. Phys. Chem. C* **2016**, *120*, 10605.
[37] C. Neumann, S. Reichardt, P. Venezuela, M. Drogeler, L. Banszerus, M. Schmitz, K. Watanabe, T. Taniguchi, F. Mauri, B. Beschoten, S. V. Rotkin, C. Stampfer, *Nat. Commun.* **2015**, *6*, 8429.

[38] H. Yan, H. Cheng, H. Yi, Y. Lin, T. Yao, C. Wang, J. Li, S. Wei, J. Lu, *J. Am. Chem. Soc.* **2015**, *137*, 10484.

[39] F. Huang, Y. Deng, Y. Chen, X. Cai, M. Peng, Z. Jia, P. Ren, D. Xiao, X. Wen, N. Wang, H. Liu, D. Ma, *J. Am. Chem. Soc.* **2018**, *140*, 4113142.

[40] Z. Chen, E. Vorobyeva, S. Mitchell, E. Fako, M. A. Ortuno, N. Lopez, S. M. Collins, P. A. Midgley, S. Richard, G. Vile, J. Perez-Ramirez, *Nat. Nanotechnol.* **2018**, *13*, 702.

[41] X. Huang, H. Yan, L. Huang, X. Zhang, Y. Lin, J. Li, Y. Xia, Y. Ma, Z. Sun, S. Wei, J. Lu, *J. Phys. Chem. C* **2018**, *123*, 7922.

[42] S. F. Hackett, R. M. Brydson, M. H. Gass, I. Harvey, A. D. Newman, K. Wilson, A. F. Lee, *Angew. Chem., Int. Ed.* **2007**, *46*, 8593.

[43] K. Layek, M. L. Kantam, M. Shirai, D. Nishio-Hamane, T. Sasaki, H. Maheswaran, *Green Chem.* **2012**, *14*, 3164.

[44] Y. Chen, X. Xie, X. Xin, Z. R. Tang, Y. J. Xu, *ACS Nano* **2019**, *13*, 295.

[45] Z. Chen, S. Liu, M. Q. Yang, Y. J. Xu, *ACS Appl. Mater. Interfaces* **2013**, *5*, 4309.

[46] C. Han, Z. Chen, N. Zhang, J. C. Colmenares, Y. J. Xu, *Adv. Funct. Mater.* **2015**, *25*, 221.

[47] S. H. Li, N. Zhang, X. Xie, R. Luque, Y. J. Xu, *Angew. Chem., Int. Ed.* **2018**, *57*, 13082.

[48] H. Wei, X. Liu, A. Wang, L. Zhang, B. Qiao, X. Yang, Y. Huang, S. Miao, J. Liu, T. Zhang, *Nat. Commun.* **2014**, *5*, 5634.

[49] H. Qi, P. Yu, Y. Wang, G. Han, H. Liu, Y. Yi, Y. Li, L. Mao, *J. Am. Chem. Soc.* **2015**, *137*, 5260.

[50] J. Xi, H. Sun, D. Wang, Z. Zhang, X. Duan, J. Xiao, F. Xiao, L. Liu, S. Wang, *Appl. Catal., B* **2018**, *225*, 291.

[51] S.-J. Liang, L. K. Ang, *Phys. Rev. Appl.* **2015**, *3*, 014002.

[52] H. Li, K. Yu, C. Li, Z. Tang, B. Guo, X. Lei, H. Fu, Z. Zhu, *Sci. Rep.* **2015**, *5*, 18730.

[53] X. H. Li, J. S. Chen, X. Wang, J. Sun, M. Antonietti, *J. Am. Chem. Soc.* **2011**, *133*, 8074.

[54] C. Tang, L. Zhong, B. Zhang, H. F. Wang, Q. Zhang, *Adv. Mater.* **2018**, *30*, 1705110.